16 × 16 Silicon Optical Switch Based on Dual-Ring-Assisted Mach–Zehnder Interferometers

Zhanzhi Guo, Liangjun Lu, Linjie Zhou, Lin Shen, and Jianping Chen

(Invited Paper)

***Abstract*—In this paper , we report a nanosecond 16 × 16 silicon electro-optic switch chip based on a Benes architecture. The switch adopts dual-ring-assisted Mach–Zehnder interferometers as the basic building blocks. In each switch element, both TiN microheaters and PIN diodes are integrated for ring resonance alignment and high-speed switching, respectively. A transfer-matrix-based theoretical model is established to analyze the switch performances. The 16 × 16 switch is characterized by measuring the optical transmission spectra and quadrature phase-shift keying (QPSK) data transmission through 16 representative optical paths. The insertion loss of the entire switch chip is 10.6 ± 1.7 dB and the crosstalk is less than −20.5 dB. The 32-Gb/s QPSK signal is successfully switched to different destination ports by reconfiguring the optical paths, verifying the signal integrity after switching.**

***Index Terms*—Mach–Zehnder interferometer (MZI), microring resonator (MRR), optical switch, silicon photonics.**

I. Introduction

DRIVEN by the growing demand in big data applications and cloud-computing, data center traffic flow is estimated to account for 77% of the data center traffic by 2020, far outpacing data center to user and data center to data center communications [1]. Datacenters need routers and switches with higher speed, lower latency and lower power consumption to accommodate ever growing data communication between servers. Similar to data centers, high-performance supercomputer systems performing tasks in parallel by interconnecting a large number of processors benefit from high speed switching networks [2]. Silicon photonics with its attractive merits of high-integration capability, compatibility with microelectronic circuits, low cost and fast response, offers the potential to enable next generation high speed optical switching networks [3]–[5]. Optical switches could also be realized using other technologies like micro-electro-mechanical-systems (MEMS) [6], [7], III-V semiconductor integration [8], [9], silica planar lightwave circuit (PLC) integration [10], [11]. Comparing to these methods, silicon optical switches have a smaller footprint and a faster response speed than the MEMS and silica switches, while they also possess lower power consumption than III-V optical switches. Recently, MEMS-actuated silicon waveguide-based switches [12], [13] have been reported, which present the attractive merits of no static power consumption and low insertion loss. However, the drive voltage is still high (>10 V) and the switching speed is in the order of MHz, which may not satisfy the fast exchange requirement for small-size data in big-data applications.

Micro-ring resonators (MRRs) [14]–[17] and Mach-Zehnder interferometers (MZIs) [18]–[27] have been widely employed in integrated photonic circuits to build a switch chip. Multiple stages of switch elements (SEs) can be cascaded to expand the scale of the switch fabric. The MZI features broadband and temperature insensitive switching. However, in order to induce a "π" phase shift to change the switching state, the modulation arms of the MZI need to be hundreds of micrometers long, which occupies a significant footprint of the switch chip. The MRR exhibits a Lorenzian line shape in the transmission spectrum, requiring a smaller phase shift to change the state. Thus, the switching power consumption is less than that of the MZI. Previously, we have successfully demonstrated 2 × 2 and 4 × 4 dual-ring assisted MZI (DR-MZI) switches [28], [29]. The DR-MZI combines the merits of both the MZI and the MRR, in that the switching extinction ratio (ER) is high due to the coherent interference by the MZI and the power consumption is low due to the resonance enhancement by the MRR.

In this work, we further extend the scale of the DR-MZI switch to a port count of 16 × 16. The difficulty in design, fabrication and test exponentially increases with the switch scale, especially for resonant switch structures. The paper is organized as follows. In Section II, we first introduce the working principle of the DR-MZI SE. A transfer matrix model is established to theoretically analyze the switch properties. In particular, its switching performance is compared to those of single-ring and coupled-ring switches. Next, the 16 × 16 switch fabric is presented and the narrowing of the passband is studied based on the model. Section III describes the fabrication and package of the switch chip. Section IV presents the experimental setup and measurement results, including the 2 × 2 DR-MZI and the entire 16 × 16 switch chip. The 3-dB optical bandwidth is 0.33 nm and crosstalk is −20.5 dB. A 32 Gb/s quadrature phase-shift keying (QPSK) signal is successfully transmitted through the chip with slightly deteriorated error vector magnitude (EVM). Section V gives the conclusions.

Manuscript received July 1, 2017; revised August 11, 2017; accepted September 5, 2017. Date of publication September 12, 2017; date of current version February 24, 2018. This work was supported in part by the National Natural Science Foundation of China (NSFC) (61422508, 61535006, 61661130155). *(Corresponding author: Linjie Zhou.)*

The authors are with the State Key Laboratory of Advanced Optical Communication Systems and Networks, Department of Electronic Engineering, Shanghai Jiao Tong University, Shanghai 200240, China (e-mail: guo_zhanzhi@sjtu.edu.cn; luliangjun@sjtu.edu.cn; ljzhou@sjtu.edu.cn; shenmumu@sjtu.edu.cn; jpchen62@sjtu.edu.cn).

Color versions of one or more of the figures in this paper are available online at http://ieeexplore.ieee.org.

Digital Object Identifier 10.1109/JLT.2017.2751562

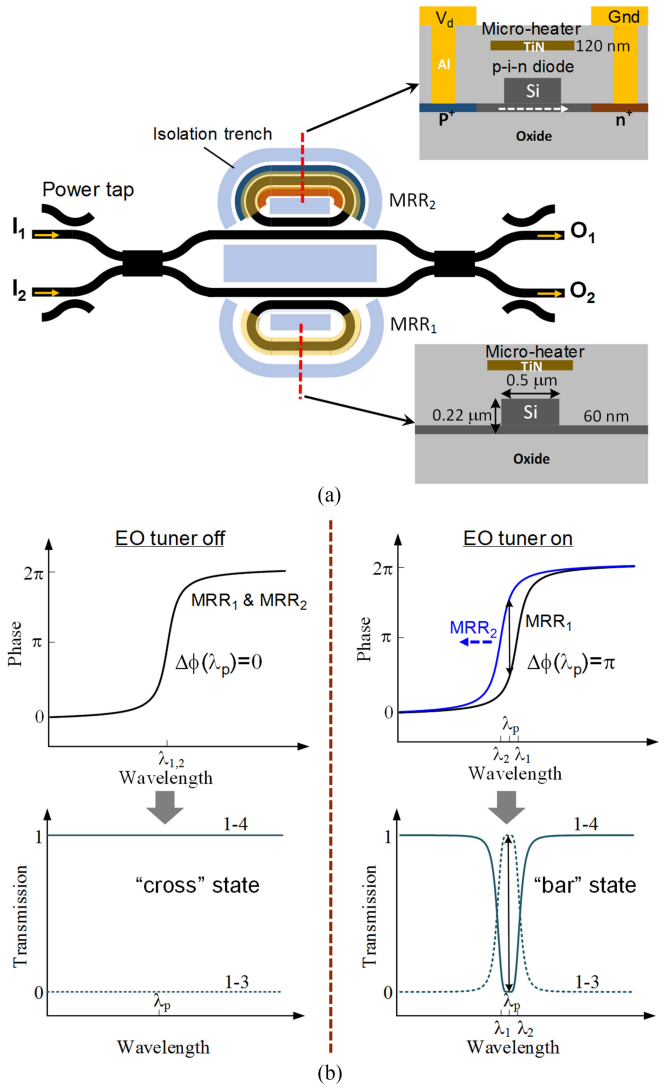

Fig. 1. (a) Schematic drawing of the 2 × 2 DR-MZI. Inset shows the cross-sections of the waveguides of the upper MRR (top right) and the bottom MRR (bottom right). (b) Switching working principle illustration. The top plots show the phase responses of the two MRR-coupled MZI arms. The bottom plots show the resultant bar-port and cross-port power transmission.

II. Switch Architecture

A. 2 × 2 DR-MZI

Although MZI switches can provide good switching performance, the active arm waveguide is still very long as a π phase shift is needed to change the switching state. To reduce the phase change and hence the power consumption, we can use a slow-light structure to replace the long arm. The phase change of a waveguide is directly related to its group refractive index. Therefore, if the group index change in a slow-light structure is very large, then the arm length required for the π phase shift can be reduced considerably. There are various slow-light structures that can be used, such as microring resonators, Bragg gratings, photonic crystals etc. Here, we choose the microring resonator for its simple structure and easy fabrication.

Fig. 1(a) shows the schematic structure of the 2 × 2 DR-MZI, which is composed of a MZI with a MRR coupled to each arm. The upper MRR is integrated with both a TiN microheater on top of the ring waveguide and a PIN diode across the waveguide. The bottom MRR is only integrated with a TiN microheater. The insets illustrate the cross-sections of the ring waveguides. We employ isolation trenches around the MRRs to reduce thermal crosstalk. The thermo-optic (TO) tuning of both MRRs ensures that the resonances can be aligned and shifted to any arbitrary wavelength. The TO effect would not result in excessive loss. The electro-optic (EO) tuning of one MRR gives the fast data exchange between the two output ports.

Fig. 1(b) explains the working principle of the DR-MZI switch. When the two MRRs with the same size and coupling coefficient resonate at the same wavelength, the two arms have identical responses, resulting in zero phase difference between them. Therefore, after interference by the MZI, the input light is transmitted to the cross port with the maximum transmission. As the MRRs are designed to work in the over-coupling regime, the MZI arm experiences a rapid phase change from 0 to 2π across the resonance wavelength. Therefore, a slight refractive index modulation to one MRR could induce a π phase difference between the two arms, changing the destination to the bar port. It should be noted that the operation wavelength should be chosen at the middle of the two resonances after EO switching, i.e., $\lambda_p = (\lambda_1 + \lambda_2)/2$. In our single-drive scheme, the operation wavelength is blue-detuned from the original resonance wavelength. If a dual-drive push-pull scheme is employed by integrating PIN diodes to both MRRs, then the operation wavelength is fixed at the original resonance wavelength. It can be easily seen that such a DR-MZI structure is actually a second-order filter. The bar-state passband exhibits a flat top and fast roll-off.

The DR-MZI can be modeled by the following transfer matrix:

$$\begin{bmatrix} E_{\text{bar}} \\ E_{\text{cross}} \end{bmatrix} = \begin{bmatrix} \tau & j\kappa \\ j\kappa & \tau \end{bmatrix} \begin{bmatrix} E_{T1} & 0 \\ 0 & E_{T2} \end{bmatrix} \begin{bmatrix} \tau & j\kappa \\ j\kappa & \tau \end{bmatrix} \begin{bmatrix} E_{\text{in}} \\ 0 \end{bmatrix} \quad (1)$$

where E_{bar}, E_{cross}, and E_{in} represent the electric fields at the bar port, the cross port, and the input port, respectively, κ and τ are the coupling and transmission coefficients of the input and output multimode interference (MMI) couplers ($\kappa^2 = \tau^2 = 0.5$ for a perfect 3-dB coupler), $E_{Ti} = T_i e^{i\phi i} (i = 1, 2)$ is the electric field transmission through the MRR-coupled MZI arm. The amplitude and phase responses T_i and φ_i are given by

$$T_i^2 = \frac{t^2 + a^2 - 2ta\cos\theta_i}{1 - 2ta\cos\theta_i + (ta)^2} \quad (2)$$

$$\varphi_i = -\arctan\left(\frac{a\sin\theta_i}{t - a\cos\theta_i}\right) + \arctan\left(\frac{ta\sin\theta_i}{1 - ta\cos\theta_i}\right) \quad (3)$$

where t is the field transmission coefficient, θ_i $(i = 1, 2)$ is the round-trip phase in the MRR, and a is the ring loss factor. The input normalized output powers at the bar and cross ports are thus expressed as

$$P_b = \left|\frac{E_{\text{bar}}}{E_{\text{in}}}\right|^2 = \frac{(T_1^2 + T_2^2 - 2T_1T_2\cos(\varphi_1 - \varphi_2))}{4} \quad (4)$$

$$P_x = \left|\frac{E_{\text{bar}}}{E_{\text{in}}}\right|^2 = \frac{(T_1^2 + T_2^2 + 2T_1T_2\cos(\varphi_1 - \varphi_2))}{4} \quad (5)$$

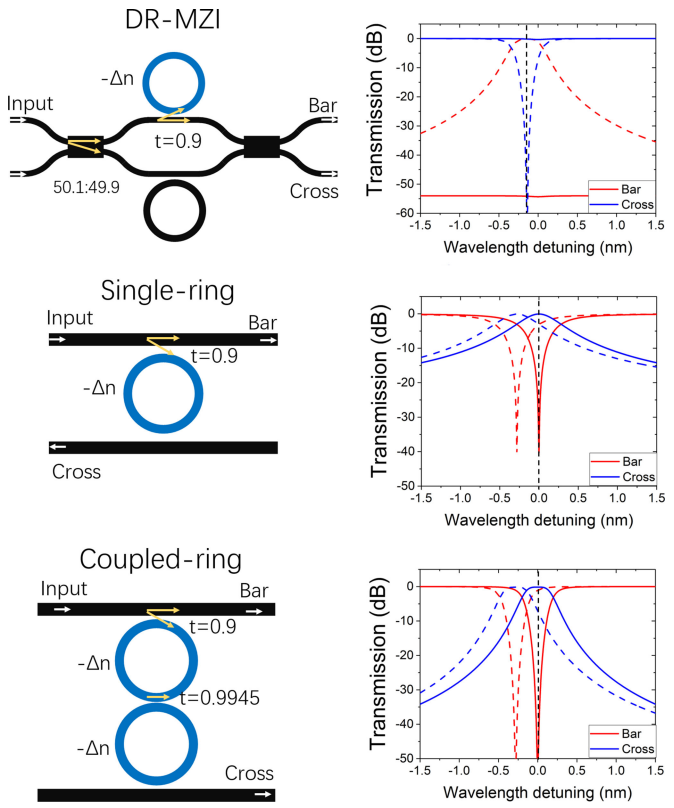

Fig. 2. Comparison of three ring resonator-based switch structures: DR-MZI, single-ring, and coupled-ring resonators. The field transmission coefficient t between the MRR and MZI arm waveguide is set as 0.9 and the ring loss factor a is 0.998. The refractive index modulation is $\Delta n = 7.31e{-}04$.

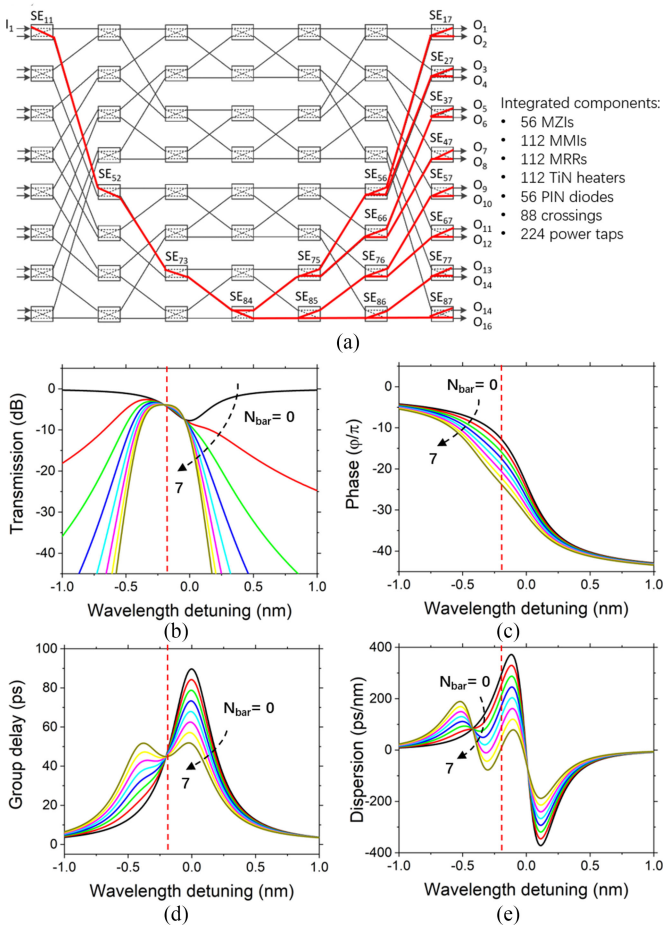

Fig. 3. (a) Topology of the 16 × 16 switch chip. The red lines highlight the light paths that we measured during the experiment. (b)–(e) Calculated spectral responses for (b) optical power, (c) phase, (d) group delay, and (e) group delay dispersion after passing seven stages of SEs with different number of bar-state SEs ($N_{bar} = 0, 1, 2 \ldots 7$). The dashed vertical red line indicates the operation wavelength.

Based on the above equations, the transmission spectrum of a DR-MZI SE can be calculated. The entire 16 × 16 switch chip can also be modeled by multiplying the transfer matrices given by (1).

We compare the DR-MZI switch with the single-MRR and coupled-MRR switches as shown in Fig. 2. The spectra are calculated using the transfer equations with the same set of design parameters, including ring size, coupling coefficient, and refractive index modulation. The switch is changed from the cross-state to the bar-state by introducing a small refractive index modulation to the MRR(s) in all three structures. It can be seen that a high switching ER can be easily obtained from both the cross and the bar ports for the DR-MZI. However, for the regular MRR switches, the small refractive index modulation is not enough to induce a large enough resonance shift. As a consequence, the ER is low or insertion loss (IL) is high for at least one port. In order to increase the ER and reduce the IL, the refractive index modulation magnitude have to be increased, inevitably leading to higher electrical power consumption.

B. 16 × 16 Switch Architecture

The 16 × 16 optical switch fabric is constructed on a Benes architecture, as shown in Fig. 3(a). It incorporates 56 DR-MZI SEs. Each light path connecting an input port to a destination output port passes through seven SEs. Connection of all 16 input and 16 output ports gives 2^{56} permutations, but only 16! of them are necessary to accommodate the complete input-to-output mapping. Compared to other commonly adopted switch topologies, like path-independent insertion-loss (PILOSS), crossbar and switch-and-select (S&S), the Benes architecture requires the least number of SEs with a low IL. This reduces the chip footprint and makes the electrical drive easier. The Benes architecture could be further improved by adopting dilated structure. In the dilated Benes network [30], the first order crosstalk results from a SE carrying two active light paths could be avoided.

As the switch matrix contains 88 waveguide junctions, we employ 90°-crossed MMIs [27] to reduce the optical loss and the crosstalk imposed by the crossings. The radius of the racetrack MRR is 10 μm. The coupling length and the gap size between the MRR and the MZI arm are designed to be 4.2 μm and 0.2 μm, respectively, to ensure the MRR works in the over-coupling regime with a broad resonance linewidth. Optical power taps terminated with local grating couplers are added to the input and output ends of the DR-MZI to facilitate the characterization of each SE prior to the chip package. The taps are made up of directional couplers with a designed power splitting ratio of 1:10.

As the DR-MZI is a resonant structure with a narrow passband in the bar-state. The cascading of multiple SEs may narrow down the passband. We calculated the optical power, phase, group delay, and group delay dispersion spectra for light travelling through an optical path in the 16 × 16 switch as shown in Fig. 3(b)–(e). The number of bar-state SEs (N_{bar}) and the

number of cross-state SEs ($N_{cross} = 7–N_{bar}$) are varied to represent different configurations of an optical path. The loss of waveguide crossings and connection waveguides was neglected. In our calculation, we assumed $a = 0.9905$ and $t = 0.86$ to match with the experimental data. One can observe that, when the SEs are all in the cross-state with EO tuners off, the output transmission spectrum exhibits a dip, originated from the intrinsic loss of the MRRs. When one SE is in the bar-state after EO tuning of one MRR, then the output spectrum presents a resonance peak blue-shifted with respect to the original resonance wavelength. As the DR-MZI works in the single-drive mode, the operation wavelength should be chosen at the blue-shifted wavelength λ_p. This could also partially reduce the all-cross transmission loss. If more SEs in the light path are changed to the bar-state, the resonance peak will become narrower with a reduced passband. This effect is taken into consideration when we choose the MRR coupling coefficient. The passband should be broad enough to allow a modulated optical signal to transmit through without cutting off the sidebands. Because the operation wavelength is chosen to be at the blue-detuned resonance wavelength, the dispersion is relatively high for the cross-state. The dispersion decreases with the increasing number of bar-state SEs.

It is noticeable that the spectrum exhibits asymmetric shape when the light path contains both cross-state and bar-state SEs, especially when there is only one bar-state SE. This is due to the single drive scheme that we used in switching. The passband is blue-shifted and its superposition with the resonance dip from the cross-state SEs gives rise to the asymmetric passband spectral profile. If a push-pull drive scheme were adopted, the operation wavelength could be fixed at the original resonance wavelength and the passband thus keeps symmetric. The second-order dispersion is zero at the operation wavelength. To realize the push-pull drive, both of the two MRRs need to be integrated with PIN diodes. The SE should be first tuned to an intermediate state where the phase difference at the operation wavelength is $\pi/2$ between the two modulation arms. Then one MRR is turned on to get 0 phase difference to reach the cross-state, or the other MRR is turned on to get π phase difference to reach the bar-state. The push-pull drive scheme improves the switch performances but it also increases the integration complexity.

III. Fabrication and Package

The fabrication of the 16 × 16 switch chip was carried out using CMOS compatible processes in IME Singapore. The SOI wafer has a top silicon layer thickness of 220 nm and a buried silicon oxide layer thickness of 2 μm. Waveguides were patterned using 248-nm deep ultra-violet (DUV) photolithography. The waveguide width in the DR-MZI is 500 nm. The width of the long connection waveguides is widened to 2 μm with a linear taper in order to reduce the waveguide transmission loss. The waveguide etch depth is 160 nm to form a rib-type structure. High-density phosphorus and boron implantation doping with a concentration of $\sim 10^{20}$ cm^{-3} was performed to the waveguide slab to form a PIN diode. Rapid thermal annealing at 1030 °C for 5 seconds was followed to activate the implanted dopants. Silicon dioxide layer with a thickness of 1.5 μm was deposited using plasma enhanced chemical vapor deposition (PECVD). Next, the TiN layer with a thickness of 120 nm was deposited and patterned to form the micro-heaters. Another 0.73 μm thick silicon dioxide layer was deposited to cover the TiN heaters.

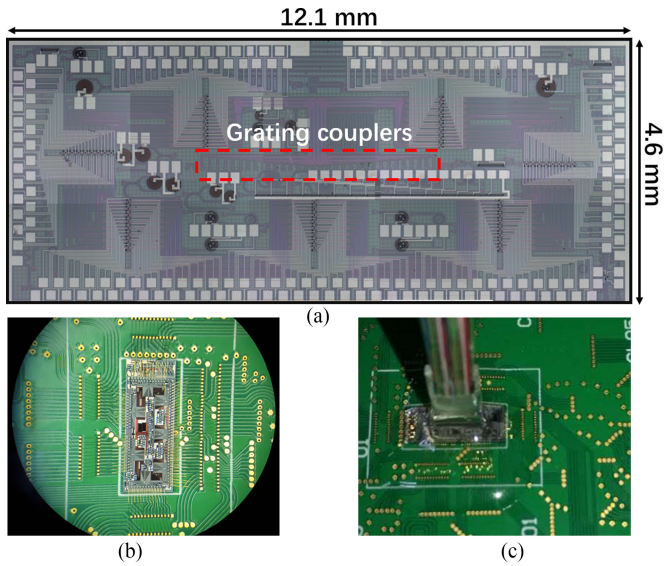

Fig. 4. (a) Microscope image of the fabricated chip. (b) Photo of the 16 × 16 switch after electrical wire-bonding. (c) Zoom-in photo of the chip after coupling with a fiber array.

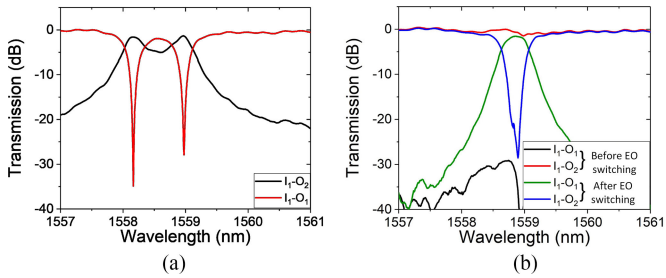

Fig. 5. Measured transmission spectra of the 2 × 2 DR-MZI (a) before TO phase error correction and (b) upon EO switching.

Finally, contact holes were etched and aluminum metal connection was formed.

Fig. 4(a) shows the microscope image of the fabricated chip. As shown in the photograph, grating couplers are located in the center of the chip for vertical coupling with a fiber array. The chip was mounted on a printed circuit board (PCB) and wire bonding was used to connect the electrical pads, as shown in Fig. 4(b). A 34-channel fiber array was aligned precisely to the grating couplers for efficient input and output coupling. Among the 34 channels, the outmost two channels were connected to a reference U-shape waveguide to facilitate fiber alignment. The fiber array was then permanently attached to the chip by ultraviolet (UV) adhesive whose refractive index is close to that of silicon dioxide. Fig. 4(c) shows the photo of the home-packaged switch chip. The coupling loss is around 6.4 dB/facet at 1550 nm after package. It should be noted that the grating couplers were not optimized for best efficiency, as we used the regular uniform grating design. The coupling efficiency could be improved using non-uniformed grating couplers [31].

IV. Experiments

A. Characterization of the DR-MZI

Fig. 5(a) shows the measured transmission spectra of the as-fabricated 2 × 2 DR-MZI. One can observe that the resonances

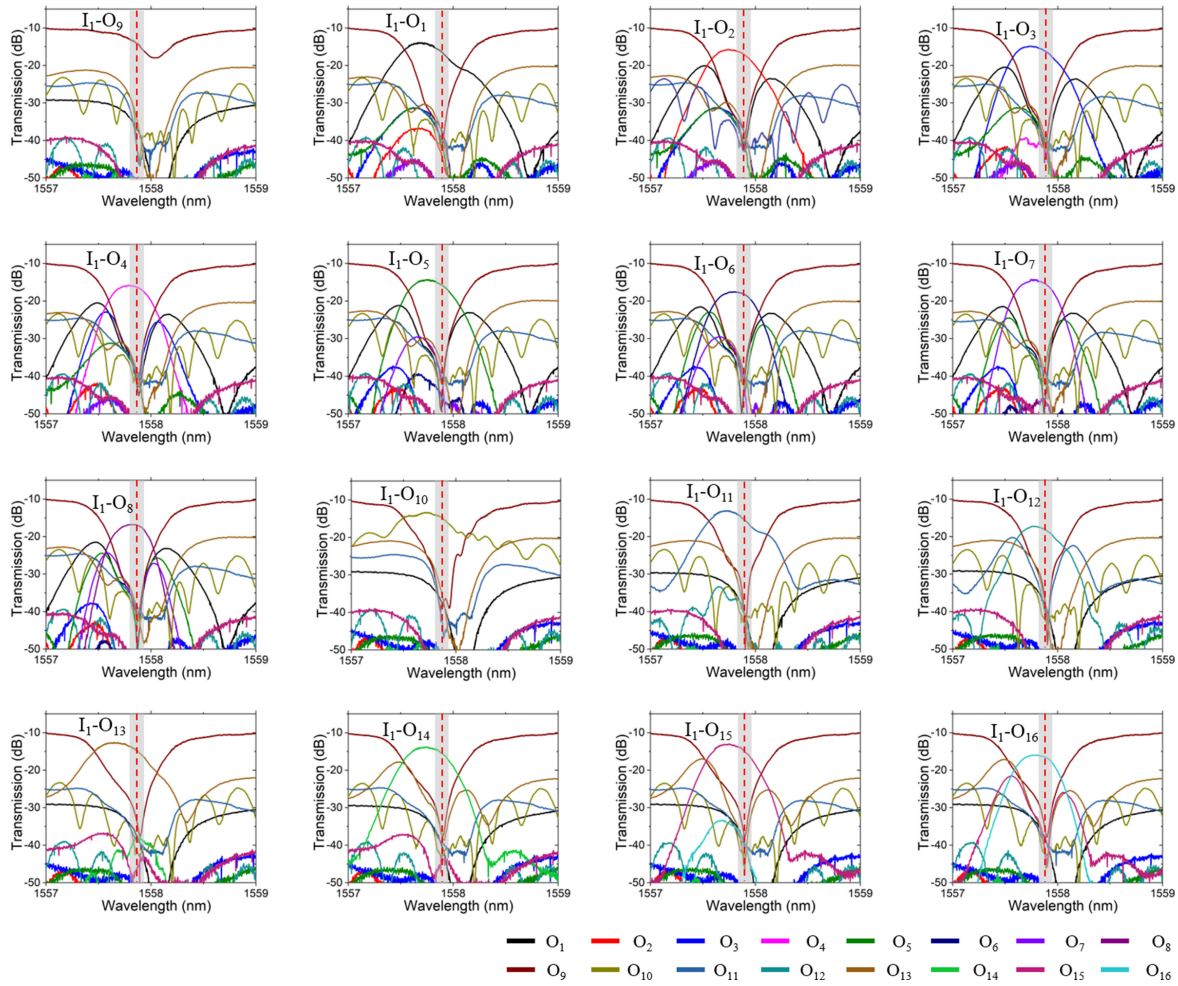

Fig. 6. Measured transmission spectra of the 16 × 16 switch. The input port is I_1 and all 16 output spectra are measured when the destination output port is switched from O_1 to O_{16}. The red dashed line indicates the operation wavelength. The grey bar represents a 16 GHz bandwidth window to accommodate the 32 Gb/s QPSK signal.

generated by the two MRRs in the DR-MZI are not aligned to the same wavelength due to fabrication errors. TO tuning was adopted to red-shift one resonance to correct the misalignment. When the resonances are aligned, the cross path ($I_1 - O_2$) reaches the maximum transmission and the bar path ($I_1 - O_1$) remains low, as illustrated in Fig. 5(b). The cross-path spectrum shows almost a flat line with only a small dip of ∼1.1 dB at the resonance wavelength of 1558.98 nm. The on-off ER between the cross and bar ports is around 30 dB, suggesting the MZI has relatively balanced optical power in the two arms. The TO tuning power consumption is 6.7 mW, as only one MRR is required to red-shift for around 0.82 nm. The TO tuning efficiency is thus extracted to be 8.2 mW/nm. To change the operation wavelength to an arbitrary target wavelength, the two MRRs need to be TO tuned simultaneously, which would consume more power.

Next, EO tuning was performed to the upper MRR. The cross-path spectrum exhibits a deep resonance notch while the bar-path presents a resonance peak at the wavelength of 1558.86 nm. The EO tuning power is only 0.28 mW. The 3-dB optical bandwidth is ∼0.45 nm, and the crosstalk is better than −27 dB. As the DR-MZI requires less carrier injection to change the switch state than the MZI does, it has a lower crosstalk than the MZI switch reported in [27].

B. Transmission Spectra of the 16 × 16 *switch*

To establish an optical path in the 16 × 16 switch, the resonances of all MRRs along that path need to be first aligned to the same wavelength using TO tuners. The DR-MZI is a resonant structure, sensitive to environment temperature variation. In order to utilize the switch chip in practical systems, various on-chip optical power monitoring schemes can be applied so that the resonance wavelength can be tracked and then locked by feedback control circuit, as demonstrated in [32]–[34]. We chose I_1 as the input port, and measured the transmission spectra from all the 16 output ports when the destination port was switched from O_1 to O_{16}.

We used a software controlled multi-channel power supply as the voltage source. The software sends out a controlling string to the voltage source through USB connection wire, once a target voltage is set. The imbedded digital-to-analog converter (DAC) chip receives a string of 2-byte data and converts it to an analogue output signal. The signal then goes through two stages of amplifiers to boost up the output voltage to drive the EO and TO tuners. The maximum output voltage is 10 V and the minimum tuning resolution is 2 mV, high enough for precise resonance control. The optical paths tested are highlighted by

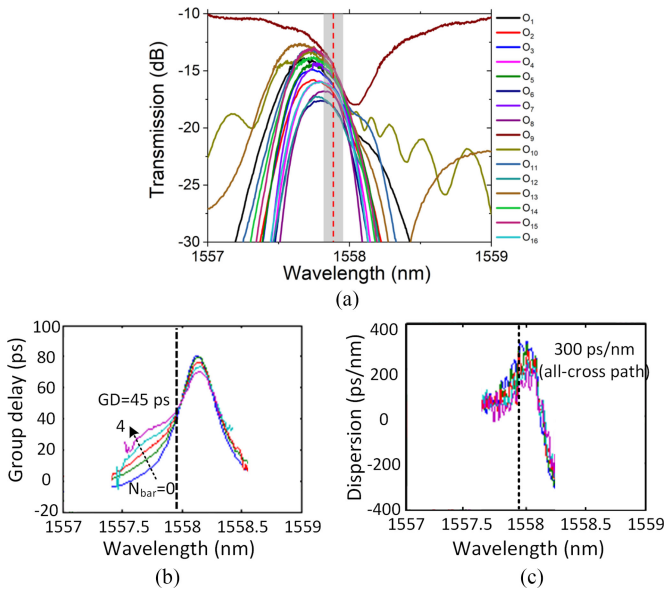

Fig. 7. (a) Transmission spectra of all 16 optical paths from I_1 to O_{1-16} lumped together. (b) Group delay and (c) group delay dispersion spectra for five typical optical paths with $N_{bar} = 0$ to 4.

red lines in Fig. 3(a). There are totally 18 SEs involved to route an optical signal from the input port I_1 to 16 output ports.

Fig. 6 shows the measured transmission spectra of all 16 optical paths. The spectra are normalized with a reference waveguide to eliminate the effect of grating couplers. When the resonances of MRRs are aligned to the wavelength of 1558.04 nm after TO tuning, light is routed to O_9 and the transmission spectrum exhibits a resonance dip of about 7.9 dB deep accumulated from the seven stages of SEs. The dip can be suppressed by reducing the round-trip loss of the MRRs and/or increasing the MRR coupling coefficient. When the EO tuning is applied to change the routing path, the dip grows into a deep notch while the central wavelength is slightly blue-shifted to 1557.89 nm. To quantify the switch performance, we define the crosstalk as the ratio of the leakage optical power to the transmitted output power at the 1557.89 nm wavelength. The worst crosstalk is observed in the path $I_1 - O_7$, where the crosstalk is around -20.5 dB.

In Fig. 7, we put all 16 transmission spectra corresponding to the 16 optical paths from I_1 to O_{1-16} together to extract the operation bandwidth and insertion loss of the switch. The path $I_1 - O_8$ exhibits the narrowest 3-dB bandwidth of around 0.33 nm, as light passes through four bar-state switching elements. The average insertion loss at 1557.89 nm is $\sim$16.2 dB with a variation of $\pm$1.7 dB. The loss includes the 5.6 dB power splitting loss from the taps, and hence, the loss due to SEs and crossings is $\sim$10.6 dB. Thus, the SE has an average insertion loss of $\sim$1.5 dB. The loss variation mainly comes from the loss difference of the DR-MZIs in the cross-state and bar-state, the different number of crossings passed and the different waveguide length in each optical path.

We choose five optical paths with the number of bar-state elements N_{bar} increasing from 0 to 4 to measure its group delay and dispersion as shown in Fig. 7(b) and (c). The measurement results are consistent with the transfer matrix calculation results in Fig. 3. The group delay is around 45 ps for all paths. The group delay dispersion has the maximum value of 300 ps/nm for the all-cross path.

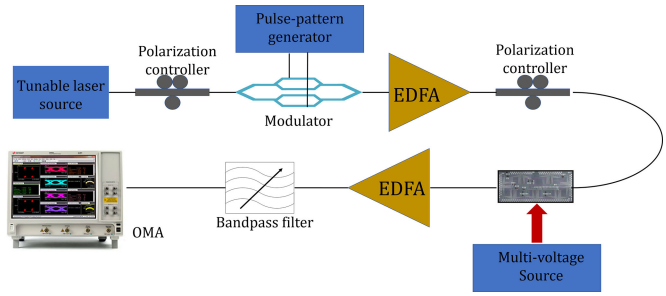

Fig. 8. System setup for QPSK data transmission experiment.

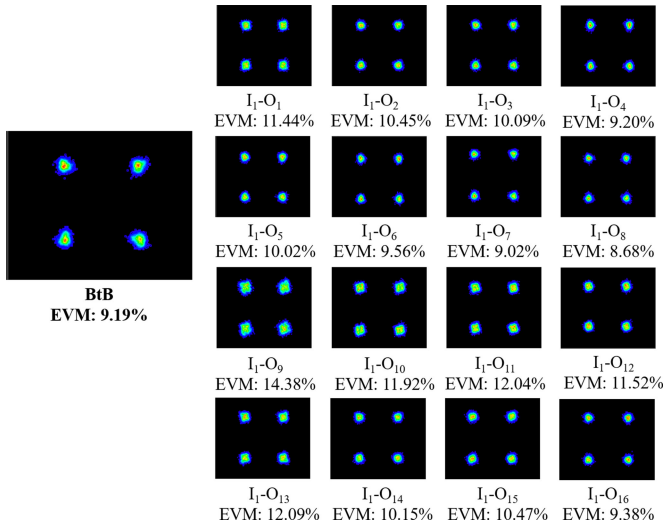

Fig. 9. Measured constellation diagrams for the BtB transmission and the 16 optical paths.

C. Switching of High-Speed QPSK Data

To verify the optical signal routing ability of the 16×16 switch, we tested the switching performance for a 32 Gb/s QPSK data stream. Fig. 8 shows the experimental setup. The laser was set to the operation wavelength of 1557.89 nm. A commercial $LiNbO_3$ in-phase and quadrature (IQ) modulator driven by a two-channel pulse pattern generator (Keysight N4951B) were used to generate the QPSK optical signal. The optical power was boosted up by an Erbium-doped fiber amplifiers (EDFA) before entering the switch chip. The out-transmitted signal from the chip was further amplified by another EDFA to compensate for the insertion loss of the chip. The output signal then went through a tunable optical bandpass filter (OBPF) with a 3-dB bandwidth of $\sim$3 nm to suppress the amplified spontaneous emission (ASE) noise before received by an optical modulation analyzer (Keysight N4932A). The received optical power was set to 0 dBm by tuning the gain of the second EDFA.

Fig. 9 shows the measured QPSK constellation diagrams for transmissions through the 16 optical paths from I_1 to O_{1-16}, together with the back-to-back (BtB) transmission. The BtB transmission was tested with the same system setup in Fig. 8 but without the switch chip. In the BtB transmission, the received optical power was also set to be 0 dBm and the bandpass filter remained as in the real data transmission measurement. The EVM of the BtB transmission is 9.19%. As the switch 3-dB passband ($\sim$0.33 nm) is larger than the QPSK signal baud

TABLE I
POWER CONSUMPTION OF THE RELEVANT SEs

SE ID	TO (mW) Upper ring	TO (mW) Bottom ring	EO (mW)
SE_{11}	3.8	6.4	Null
SE_{17}	4.7	7.6	0.36
SE_{27}	8.5	10.1	0.33
SE_{37}	10.3	7.5	0.34
SE_{47}	11.8	9.8	0.32
SE_{52}	32.0	20.5	Null
SE_{56}	15.2	10.5	0.35
SE_{57}	11.9	10.3	0.30
SE_{66}	14.4	13.1	0.37
SE_{67}	7.2	7.7	0.33
SE_{73}	37.5	23.8	Null
SE_{75}	27.5	15.2	0.30
SE_{76}	17.7	12.5	0.28
SE_{77}	9.5	6.2	0.40
SE_{84}	17.9	9.4	0.36
SE_{85}	24.5	15.9	0.34
SE_{86}	16.7	12.5	0.32
SE_{87}	8.9	8.2	0.36

rate (16 Gbaud/s), the transmitted signal does not deteriorate significantly compared to the BtB transmission.

The optical path $I_1 - O_9$ contains only cross-state SEs. As the operation wavelength is at the left slope of the dip in the transmission spectrum as seen from Fig. 6, the EVM increases to 14.38%. This is primarily due to the dispersion as revealed in Fig. 3(e). The optical paths $I_1 - O_1$, $I_1 - O_{10}$, $I_1 - O_{11}$, and $I_1 - O_{13}$ incorporate only one bar-state SE, and therefore, the constellation diagrams exhibit a comparable EVM around 11%∼12%. One can observe that the EVM improves when more switching elements are in the bar-state which agrees with the calculated dispersion trend in Fig. 3(e). The best case is obtained for the path $I_1 - O_8$, which contains four bar-state SEs. The measured EVM is 8.68%, which is even slightly better than the BtB transmission. We attribute the slight improvement of EVM to the narrow passband of this optical path that more effectively eliminates the ASE noise.

D. Power Consumption

The power consumption of the switch chip comes from two parts: the TO tuners for phase correction and the EO tuners for switching. Table I lists the power consumption values for all TO and EO tuners that are involved in optical paths $I_1 - O_{1-16}$.

Because of the relatively large unpredictable deviation of the MRR resonances from the target wavelength, the TO tuning power varies from 3.8 to 37.5 mW. The fabrication errors can be corrected by post-fabrication trimming technologies [35] or using advanced fabrication tools with a higher accuracy [36]. In that case, the TO power consumption can be reduced. The average EO tuning power is 0.34 mW, which is one order smaller than the EO tuning power of MZI based switches [27].

E. Switching Speed

The temporal response of the switch was measured on a stand-alone SE to verify the dynamic switching performance of the switch fabric. The SE was first set to the cross-state and the laser wavelength was tuned to the operation wavelength of SE. Next, a square wave RF signal with a period of about 171 ns and a duty cycle of 0.5 generated by a pulse pattern generator (Keysight N4951B) was applied to the SE by a high-speed RF probe. The modulated optical output of the SE is then amplified by an EDFA followed by a bandpass filter. The optical signal was finally received by a photodetector and the waveform was measured by an oscilloscope (Keysight MSOS804A).

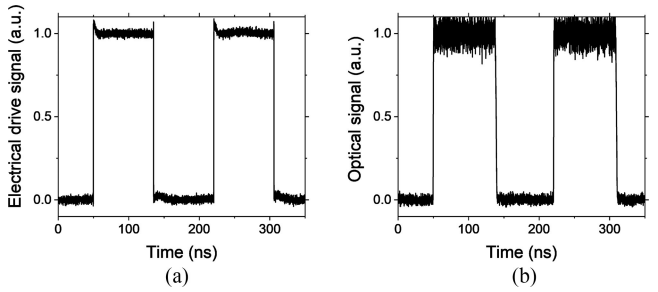

Fig. 10. (a) Electrical drive voltage waveform from the PPG. (b) Modulated optical waveform of a stand-alone SE.

The normalized electrical and optical waveforms are shown in Fig. 10. The peak-to-peak voltage of the square wave electrical signal is 0.58 V with a DC bias voltage of 0.78 V. The 10%–90% rise and fall time was measured to be 450 ps and 1.65 ns, respectively.

V. CONCLUSION

A 16×16 silicon DR-MZI EO switch based on the Benes topology was designed, fabricated and experimentally demonstrated. Each DR-MZI switching element is integrated with two TO phase shifters and one EO phase shifter for resonances alignment and switching, respectively. The transmission spectrum measurement shows that the crosstalk is better than −20.5 dB at 1557.89 nm. The on-chip insertion loss is around 10.6 ± 1.7 dB, excluding the 5.6 dB loss from the power taps. The optical 3-dB bandwidth is around 0.33 nm. Exchange of a QPSK signal among 16 optical paths has been successfully demonstrated at the bit rate of 32 Gb/s. The EVM is deteriorated by 5.2% for the worst case. The average EO power consumption of the SEs is 0.34 mW. The switch response time is in the order of nanosecond. These results represent a significant step towards the realization of integrated wavelength-selective optical switches which can find potential applications in future optical interconnection networks for datacenters and supercomputers. Moreover, because of its reconfigurability, such a switch chip can be further exploited for agile on-chip optical signal processing, such as optical filtering, phased array steering and logic operation that are worth future exploration.

REFERENCES

[1] Cisco, *Global Cloud Index: Forecast and Methodology, 2015–2020*. 2016. [Online]. Available: http://www.cisco.com/c/dam/en/us/solutions/collateral/service-provider/global-cloud-index-gci/white-paper-c11-738085.pdf

[2] A. Biberman and K. Bergman, "Optical interconnection networks for high-performance computing systems," *Rep. Prog. Phys.*, vol. 75, no. 4, pp. 046402-1–046402-15, Mar. 2012.

[3] D. Nikolova *et al.*, "Scaling silicon photonic switch fabrics for data center interconnection networks," *Opt. Exp.*, vol. 23, pp. 1159–1175, Jan. 2015.

[4] S. Nakamura, S. Yanagimachi, H. Takeshita, A. Tajima, T. Hino, and K. Fukuchi, "Optical switches based on silicon photonics for ROADM application," *IEEE J. Sel. Topics Quantum Electron.*, vol. 22, no. 6, pp. 185–193, Nov./Dec. 2016.
[5] Y. Li, Y. Zhang, L. Zhang, and A. W. Poon, "Silicon and hybrid silicon photonic devices for intra-datacenter applications: State of the art and perspectives [Invited]," *Photon. Res.*, vol. 3, pp. B10–B27, Oct. 2015.
[6] J. Kim *et al.*, "1100 × 1100 port MEMS-based optical crossconnect with 4-dB maximum loss," *IEEE Photon. Technol. Lett.*, vol. 15, no. 11, pp. 1537–1539, Oct. 2003.
[7] M. Mizukami *et al.*, "128 × 128 three-dimensional MEMS optical switch module with simultaneous optical path connection for optical cross-connect systems," *Appl. Opt.*, vol. 50, pp. 4037–4041, Jul. 2011.
[8] R. Stabile, A. Rohit, and K. Williams, "Monolithically integrated 8 × 8 space and wavelength selective cross-connect," *J. Lightw. Technol.*, vol. 32, no. 2, pp. 201–207, Jan. 2014.
[9] M. J. Kwack, T. Tanemura, A. Higo, and Y Nakano, "Monolithic InP strictly non-blocking 8 × 8 switch for high-speed WDM optical interconnection," *Opt. Exp.*, vol. 20, pp. 28734–28741, Dec. 2012.
[10] Y. Zha, D. G. Sun, T. G. Liu, Y. Zhang, X. Li, and X. Fu, "Rearrangeable nonblocking 8 × 8 matrix optical switch based on silica waveguide and extended banyan network," *IEEE Photon. Technol. Lett.*, vol. 19, no. 6, pp. 390–392, Mar. 2007.
[11] T. Shibata *et al.*, "Silica-based waveguide-type 16 × 16 optical switch module incorporating driving circuits," *IEEE Photon. Technol. Lett.*, vol. 15, no. 5, pp. 1300–1302, Sep. 2003.
[12] T. J. Seok, N. Quack, S. Han, R. S. Muller, and M. C. Wu, "Highly scalable digital silicon photonic MEMS switches," *J. Lightw. Technol.*, vol. 34, no. 2, pp. 365–371, Jan. 2016.
[13] T. J. Seok, N. Quack, S. Han, R. S. Muller, and M. C. Wu, "Large-scale broadband digital silicon photonic switches with vertical adiabatic couplers," *Optica*, vol. 3, no. 1, pp. 64–70, Jan. 2016.
[14] N. Sherwood-Droz *et al.*, "Optical 4 × 4 hitless silicon router for optical networks-on-chip (NoC)," *Opt. Exp.*, vol. 16, pp. 15915–15922, Sep. 2008.
[15] H. Jia *et al.*, "Five-port optical router based on silicon microring optical switches for photonic networks-on-chip," *IEEE Photon. Technol. Lett.*, vol. 28, no. 9, pp. 947–950, May 1, 2016.
[16] Q. Li *et al.*, "Single microring-based 2 × 2 silicon photonic crossbar switches," *IEEE Photon. Technol. Lett.*, vol. 27, no. 18, pp. 1981–1984, Sep. 2015.
[17] V. Vujicic *et al.*, "Software-defined silicon-photonics-based metro node for spatial and wavelength superchannel switching," *J. Opt. Commun. Netw.*, vol. 9, no. 5, pp. 342–350, May 2017.
[18] L. Qiao, W. Tang, and T. Chu, "32 × 32 silicon electro-optic switch with built-in monitors and balanced-status units," *Sci. Rep.*, vol. 7, p. 42306, Feb. 2017.
[19] D. Celo *et al.*, "32 × 32 silicon photonic switch," presented at the *Opto-Electronics Communications Conf.*, 2016, Paper WF1–4.
[20] L. Qiao, W. Tang, and T. Chu, "16 × 16 Non-blocking silicon electro-optic switch based on Mach-Zehnder interferometers," presented at the *Optical Fiber Communications Conf.*, 2016, Paper Th1C. 2
[21] N. Dupuis *et al.*, "Nanosecond-scale Mach–Zehnder-based CMOS photonic switch fabrics," *J. Lightw. Technol.*, vol. 35, no. 4, pp. 615–623, Feb. 2017.
[22] N. Dupuis *et al.*, "Modeling and characterization of a nonblocking 4 × 4 Mach–Zehnder silicon photonic switch fabric," *J. Lightw. Technol.*, vol. 33, no. 20 pp. 4329–4337, Oct. 2015.
[23] X. Jiejiang *et al.*, "Nonblocking 4 × 4 silicon electro-optic switch matrix with low power consumption," *IEEE Photon. Technol. Lett.*, vol. 27, no. 13, pp. 1434–1436, Jul. 2015.
[24] K. Tanizawa *et al.*, "Ultra-compact 32 × 32 strictly-non-blocking Si-wire optical switch with fan-out LGA interposer," *Opt. Exp.*, vol. 23, no. 13, pp. 17599–17606, 2015.
[25] L. Lu, L. Zhou, Z. Li, X. Wan, and J. Chen, "Broadband 4 × 4 nonblocking silicon electrooptic switches based on Mach–Zehnder interferometers," *IEEE Photon. J.*, vol. 7, no. 1, pp. 1–8, Feb. 2015.
[26] S. Zhao, L. Lu, L. Zhou, D. Li, Z. Guo, and J. Chen, "16 × 16 silicon Mach-Zehnder interferometer switch actuated with waveguide microheaters," *Photon. Res.* vol. 4, pp. 202–207, 2016.
[27] L. Lu *et al.*, "16 × 16 non-blocking silicon optical switch based on electro-optic Mach-Zehnder interferometers," *Opt. Exp.*, vol. 24, no. 9, pp. 9295–9307, May 2016.
[28] L. Lu, L. Zhou, X. Li, and J. Chen, "Low-power 2 × 2 silicon electro-optic switches based on double-ring assisted Mach–Zehnder interferometers," *Opt. Lett.*, vol. 39, no. 6, pp. 1633–1636, Mar. 2014.
[29] L. Lu *et al.*, "4 × 4 silicon optical switches based on double-ring-assisted Mach–Zehnder interferometers," *IEEE Photon. Technol. Lett.*, vol. 27, no. 23, pp. 2457–2460, Dec. 2015.
[30] K. Padmanabhan and A. Netravali, "Dilated networks for photonic switching," *IEEE Trans. Commun.*, vol. 35, no. 12, pp. 1357–1365, Dec.1987.
[31] L. He *et al.*, "A high-efficiency nonuniform grating coupler realized with 248-nm optical lithography," *IEEE Photon. Technol. Lett.*, vol. 25, no. 14, pp. 1358–1361, Jul. 2013.
[32] Y. Li and A. W. Poon, "Actively stabilized silicon microrings with integrated surface-state-absorption photodetectors using a slope-detection method," *Opt. Exp.*, vol 24, no. 19, pp. 21286–21300, Sep. 2016.
[33] K. Padmaraju, D. Logan, T. Shiraishi, J. Ackert, A. Knights, and K. Bergman, "Wavelength locking and thermally stabilizing microring resonators using dithering signals," *J. Lightw. Technol.*, vol. 32, no. 3, pp. 505–512, Feb. 2014.
[34] D. Li, L. Zhou, L. Lu, and J. Chen, "Optical power monitoring with ultrahigh sensitivity in silicon waveguides and ring resonators," *IEEE Photon. J.*, vol. 9, no. 5, pp. 1–10, Oct. 2017.
[35] A. H. Atabaki, A. A. Eftekhar, M. Askari, and A. Adibi, "Accurate post-fabrication trimming of ultra-compact resonators on silicon," *Opt. Exp.*, vol. 21, no. 12, pp. 14139–14145, Jun. 2013.
[36] S.-H. Jeong *et al.*, "Low-loss, flat-topped and spectrally uniform silicon-nanowire-based 5th-order CROW fabricated by ArF-immersion lithography process on a 300-mm SOI wafer," *Opt. Exp.*, vol. 21, no. 25, pp. 30163–30174, Dec. 2013

Zhanzhi Guo received the B.S. degree in telecommunication engineering from Xidian University, Xi'an, China, in 2014. He is currently working toward the Master degree with the State Key Laboratory of Advanced Optical Communication Systems and Networks, Department of Electronic Engineering, Shanghai Jiao Tong University, Shanghai, China. His research interests include silicon optical switches and optical communication systems.

Liangjun Lu received the B.S. degree from the Department of Optical Engineering, Zhejiang University, Hangzhou, China, in 2011, the Ph.D. degree in electronical engineering at the Shanghai Jiao Tong University, Shanghai, China. He is currently a tenure-track Assistant Professor at the State Key Laboratory of Advanced Optical Communication Systems and Networks, Shanghai Jiao Tong University, Shanghai, China. His research interests include silicon optical switches and silicon programmable optical processors etc.

Linjie Zhou received the B.S. degree in microelectronics from Peking University, Beijing, China, in 2003, and the Ph.D. degree in electronic and computer engineering from the Hong Kong University of Science and Technology, Clear Water Bay, Hong Kong, in 2007. From 2007 to 2009, he was a Postdoctoral Researcher at the University of California, Davis, CA, USA. He is currently a Professor at the State Key Laboratory of Advanced Optical Communication Systems and Networks, Shanghai Jiao Tong University, Shanghai, China. His research interests include silicon photonics, photonics integration, and plasmonic waveguide devices etc.

Lin Shen received the B.S. degree in communication engineering from Shanghai University, Shanghai, China, in 2016. She is currently working toward the master degree with the State Key Laboratory of Advanced Optical Communication Systems and Networks, Department of Electronic Engineering, Shanghai Jiao Tong University, Shanghai, China.

Jianping Chen received the B.S. degree from Zhejiang University, Hangzhou, China, in 1983, and the M.S. and Ph.D. degrees from Shanghai Jiao Tong University, Shanghai, China, in 1986 and 1992, respectively, where he is currently a Professor with the State Key Laboratory of Advanced Optical Communication Systems and Networks, Department of Electronic Engineering. His main research interests include photonic devices and signal processing, optical networking, and sensing optics. He is also a Principal Scientist of the 973 projects in China.